Bioactive Materials 36 (2024) 551–564

Contents lists available at ScienceDirect

Bioactive Materials

journal homepage: www.keaipublishing.com/en/journals/bioactive-materials

Tuning zinc content in wollastonite bioceramic endowing outstanding angiogenic and antibacterial functions beneficial for orbital reconstruction

Yiyu Peng [a], Menglu Chen [a], Jingyi Wang [a], Jiajun Xie [a], Changjun Wang [a], Xianyan Yang [b], Xiaoling Huang [a], Zhongru Gou [b,**], Juan Ye [a,*]

[a] Eye Center, The Second Affiliated Hospital, Zhejiang University School of Medicine, Zhejiang, Provincial Key Lab of Ophthalmology, Hangzhou, 310009, China
[b] Bio-nanomaterials and Regenerative Medicine Research Division, Zhejiang-California International Nanosystem Institute, Zhejiang University, Hangzhou, 310058, China

ARTICLE INFO

Keywords:
Zinc doping
Antibacterial
Angiogenesis
Wollastonite bioceramic
Orbital reconstruction

ABSTRACT

Prosthetic eye is indispensable as filler after enucleation in patients with anophthalmia, whereas there are still many complications including postoperative infection and eye socket depression or extrusion during the conventional artificial eye material applications. Some Ca-silicate biomaterials showed superior bioactivity but their biological stability *in vivo* limit the biomedical application as long-term or permanent implants. Herein we aimed to understand the physicochemical and potential biological responses of zinc doping in wollastonite bioceramic used for orbital implants. The wollastonite powders with different zinc dopant contents (CSi-Zn*x*) could be fabricated as porous implants with strut or curve surface pore geometries (cubic, IWP) via ceramic stereolithography. The experimental results indicated that, by increasing zinc-substituting-Ca ratio (up to 9%), the sintering and mechanical properties could be significantly enhanced, and meanwhile the bio-dissolution *in vitro* and biodegradability *in vivo* were thoroughly inhibited. In particular, an appreciable angiogenic activity and expected antibacterial efficacy (over 90 %) were synergistically achieved at 9 mol% Zn dopant. In the back-embedding and enucleation and implantation model experiments in rabbits, the superior continuous angiogenesis was corroborated from the 2D/3D fibrovascular reconstruction in the IWP-pore CSi–Zn9 and CSi–Zn13.5 groups within very short time stages. Totally, the present silicate-based bioceramic via selective Zn doping could produce outstanding structural stability and bifunctional biological responses which is especially valuable for developing the next-generation implants with vascular insertion and fixation in orbital reconstruction prothesis.

1. Introduction

Eyeball enucleation due to tumors, trauma, glaucoma, endophthalmitis and other diseases is an extremely delicate surgery, and the preparation of a suitable replacement prosthesis is important for the precision of surgical procedure, which is a major challenge in the clinic. Enucleation can lead to serious changes in the internal structure of the orbit, which can easily lead to abnormalities in the anatomical and physiological relationship between the socket and the prosthesis. The implant of the prosthetic eye is applied to replace the volume of the original eye contents and support the remaining eyelid to maintain normal function and appearance. Hence, a prosthesis with good interaction behavior with the implant environment is particularly important.

Nowadays orbital implants are mainly divided into natural and synthetic materials such as biogenic hydroxyapatite (HA) [1,2] and high-density polyethylene (Medpor®) [3]. However, the former have been shown to be associated with serious postoperative infection sequelae, such as *Aspergillus* and conjunctival dehiscence [4]. Also, the

Peer review under responsibility of KeAi Communications Co., Ltd.

* Corresponding author. Eye Center, The Second Affiliated Hospital, Zhejiang University School of Medicine, Zhejiang Provincial Key Laboratory of Ophthalmology, Zhejiang Provincial Clinical Research Center for Eye Diseases, Zhejiang Provincial Engineering Institute on Eye DiseasesNo.88 Jiefang Rd, Hangzhou, 310009, China.

** Corresponding author. Zhejiang-California International NanoSystems Institute Zhejiang University, Yuhangtang Road 866, Hangzhou 310058, China.

E-mail addresses: 11918410@zju.edu.cn (Y. Peng), 0621644@zju.edu.cn (M. Chen), wangjy0815@zju.edu.cn (J. Wang), jiajunxie@zju.edu.cn (J. Xie), wangchangjun@zju.edu.cn (C. Wang), xyyang2008@zju.edu.cn (X. Yang), huang_xiaoling@zju.edu.cn (X. Huang), zhrgou@zju.edu.cn (Z. Gou), yejuan@zju.edu.cn (J. Ye).

https://doi.org/10.1016/j.bioactmat.2024.02.027
Received 27 November 2023; Received in revised form 14 February 2024; Accepted 23 February 2024

fibrovascularization effect of Medpor implantation is suboptimal unless it is equipped with allogeneic stem cells and fibrin which comes with immune rejection and postoperative infection [5]. On the other hand, the patients often suffer from ptosis, eyelid retraction, eye socket depression after surgery, and need to be corrected by a second operation due to orbital fat atrophy by low biocompatibility of implants [6]. It is reported that some patients meet with shrinking orbital implant after HA implantation due to unexpected degradation [7]. Therefore, the development of customized multifunctional orbital implants to achieve better clinical outcomes represents a necessary topic of research.

Among the relevant features of orbital prosthesis, fast and adequate fibro-vascularization is essential for short-term implantation, especially in the case of steel-nail-fixation-free surgery, which can improve the movement of prosthesis according to some clinical outcomes [8,9]. In general, the orbital bioceramics came from dental surgery or bone defect reconstruction areas [10–14], as well as ophthalmology application [15,16]. Wollastonite ($CaSiO_3$; CSi), known as one of Ca-silicate bioceramics, has been widely investigated in a variety of biomedical application [17–23]. The osteogenic and immunomodulatory performances of such silicate-based bioceramics have been further studied by foreign ion doping, including zinc [24], magnesium [25,26], copper [27] for bone tissue engineering. In contrast, it is evident that the fibro-vascularization and antibacterial potential are the most requirements in orbital reconstruction. Among these biologically essential functional metal ions, zinc ions have been proved to have excellent antibacterial property [28], angiogenesis, and vascular functionalization [29–31] as well as the ability to accelerate wound healing [32]. Therefore, the functional ion doping may be a promising approach to develop the new generation of orbital reconstruction implants.

Over the past decade, the material selection criteria for prosthetic eyes have evolved from primitive non-porous polymer spheres to those with more complex morphology and appearance, making clinical reliability over a long term. There are evidences that the porous implants have excellent motility in the eyeball enucleation applications [33]. In this aspect, The 3D printing technology may allow porous bioceramic implants for fast angiogenesis [34,35]. It is reasonable to assume that, indeed, there are a time-consuming and complex process to design the customized porous implants with expected microstructures to balance the characteristics of pore geometry, porosity and structural stability. On the other hand, it is considered that pore geometry and stress distribution are critical for permanent orbital reconstruction due to their intrinsic mechanical weakness and brittleness during degradation. It is difficult to predict the stress change of different pore geometries, and meanwhile the fibro-vascularization is also affected by these structural parameters.

Based on the above concerns, herein we aimed to investigate the effect of Zn dopant on the sintering and mechanical properties of wollastonite bioceramic. With Schoen's I-graph-wrapped package (IWP) and cubic pore structures fabricated by computer-aided design and ceramic stereolithography, we further explored the relationship between Zn content and potential biological performances of such Zn-doped wollastonite (CSi–Zn) bioceramic implants. Moreover, the biological responses of porous implants were evaluated in the rabbit enucleation model and the anti-inflammatory, antibacterial and fibro-vascularization ability after implantation was studied, in comparison with the clinical used HA and Medpor® implants. We concluded that tuning Zn content in wollastonite bioceramic could significantly retard biodegradation and endow appreciable angiogenic acceleration and antibacterial potential *in vivo*. This newly developed orbital implants will provide ophthalmologists a more prospective choice in clinical eyeball enucleation prothesis.

2. Methods and materials

2.1. Materials and reagents

Analytical grade reagents including calcium nitrate tetrahydrate ($Ca(NO_3)_2{\cdot}4H_2O$), sodium silicate hexahydrate ($Na_2SiO_3{\cdot}9H_2O$), zinc nitrate hexahydrate ($Zn(NO_3)_2{\cdot}6H_2O$) were purchased from Sinopharm Group Chemical Reagent Co., LTD. The reagent photosensitive resin was purchased from Beijing Ten-dimensional Technology Co., LTD. The porous HA prosthetic implant was purchased from Puchuan Biological Co., LTD., and the MEDPOR@ Surgical Implant was purchased from Stryker Lebinger GmbH&Co. KG. The original size was 18 mm diameter, and was cut into 12 mm diameter by sterile surgical instrument to fit the rabbit eye socket during the enucleation implant surgery.

2.2. Preparation of bioceramic scaffolds

The co-precipitated Zn-doped calcium silicate (CSi-Zn*x*) powders were synthesized by partially replacing the original calcium nitrate with zinc nitrate according to the ratio (*x*) of 4.5, 9.0, 13.5 mol% while the other conditions remained the same, as the previous report [36] (Scheme 1). The calcined bioceramic powder was ground in a planetary ball mill until the particle size was smaller than 5 μm. The bioceramic discs (Ø 10 × 2 mm) were firstly prepared through compression process for cell and bacteria culture experiments *in vitro*. Then, the bioceramic powder was mixed with the photosensitive resin by mechanical stirring according to the ratio of 20 g/10 mL, and printed by digital light processing (DLP) 3D printer [37]. The 3D printing cylindrical porous models (Ø 10 × 5 mm, 6 × 8.5 mm; n = 3) with cubic pores were constructed by Materialise Magics 21.0 software based on a cubic cell unit with pore size of 500 μm for the primary mechanical tests. As for the physical characteristics of multiple orbital implant tests and ectopic back subcutaneous embedding experiment *in vivo*, the cylindrical porous models (Ø 10 × 5 mm, 6 × 8.5 mm; n = 3) with cubic or IWP pores with pore size of 500 μm were applied. The CSi–Zn9 and CSi–Zn13.5 scaffold samples with skeleton-IWP or cubic pores were denoted respectively as Zn9-IWP, Zn9-Cubic, Zn13.5-IWP, and Zn13.5-Cubic for subsequent tests. Meanwhile, the spherical implants (Ø 6 mm) with cubic or IWP unit cell were printed for enucleation and prosthesis implantation surgery. The printed bodies were washed in deionized water by ultrasonic oscillator, dried in an oven at 60 °C, and then calcined in a micro-controller-regulated temperature Muffle furnace (Kejing Co., Hefei, Anhui, China) at an exact heating rate of 2 °C/min. In particular, the compressive strength and compressive modulus of the four groups of bioceramic scaffolds were detected at the maximum sintering temperature condition of 1050, 1150 and 1250 °C, respectively.

2.3. Primary physicochemical, mechanical and structure tests

The chemical compositions of the bioceramic powders were detected by Inductive Coupled Plasma Emission Spectrometer (ICP; Thermo, UK), and the crystal phase were detected by X-ray diffraction (XRD, Rigaku Co., Japan). Morphological and structural characterizations of sintered samples were examined by scanning electron microscopy (SEM; GEMINI 300, ZEISS, Germany). The compression performance of cylindrical scaffold (Ø 6.0 × 8.5 mm; n = 3) was measured by universal testing machine (Instron 5566). The deformation range of the sample in the test is 0~8.5 mm, and the force change range is 0~2000 N. The test loading speed is 0.5 mm/min, and the output deformation curve can be directly obtained through automatic data collection by the computer. The corresponding stress-strain curves were plotted by Origin 2024 software. The COMSOL Multiphysics software was used to analyze and calculate the permeability of computational fluid dynamics (CFD) simulation model. Due to the symmetry of the structure, only 1.5 × 1.5 × 1.5 mm units are used for analysis. When calculating, the inlet velocity is set to 0.1 mm/s, the outlet pressure is set to 0, the fluid density is set to 1050

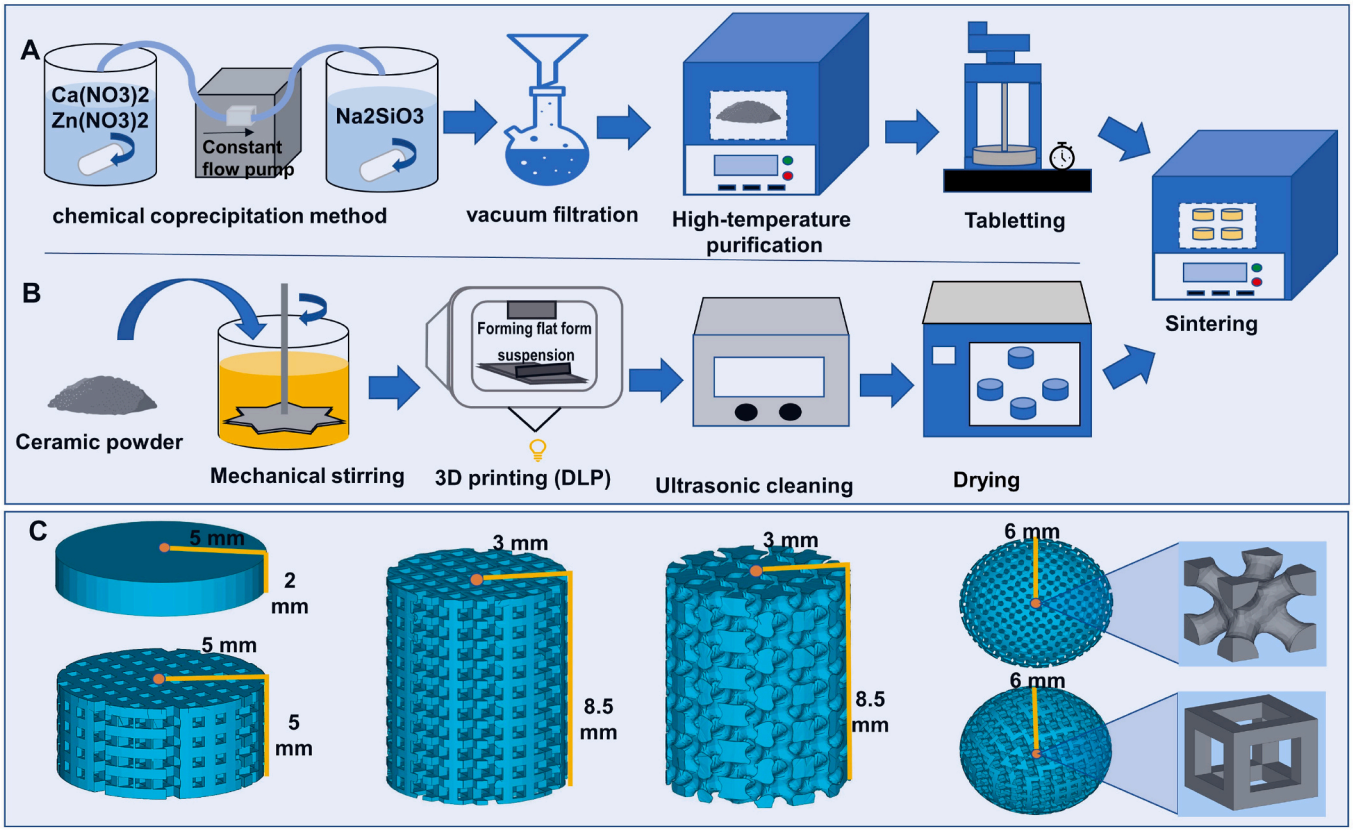

Scheme 1. Bioceramic powder preparation and bioceramic sample fabrication. (A) Synthesis of bioceramic CSi-Zn*x* powders. (B) Bioceramic scaffold printing and sintering treatment. (C) The non-porous disc, porous cylindrical, and spherical 3D models and pore unit cell models of bioceramic samples.

kg/m^3, and the viscosity is set to 0.0037 kg/m/s. The Darcy's law defined in the following equation was applied to calculate the effective permeability:

$$K = \frac{v\mu L}{\Delta P}$$

Where K represents effective permeability (m^2), v represents the inlet fluid flow velocity (m/s), μ represents dynamic fluid viscosity (kg/m/s), L represents model length (m), and ΔP represents pressure difference (MPa).

2.4. *In vitro* bio-dissolution evaluation

The degradation behavior of the materials *in vitro* was detected by Tris buffer (pH 7.4) immersion test in the incubator at 37 °C. The supernatant (0.5 mL per sample) was sampled according to the time points during 1–42 days of soaking. Calcium, silicon and zinc ions were detected by ICP test. The soaking buffer was renewed every week in the proportion of 20% to replace the fresh Tris solution, and the pH of the 20% original solution removed was measured and recorded. At 1–6 weeks, the mass loss was also detected. The scaffold mass test was carried out after rinsed with deionized water and anhydrous ethanol and dried at 60 °C for 12 h. The compression test was also performed after the *in vitro* degradation test. The non-contact optical profiler (WykoNT9100, Veeco, America) was employed to detect the surface roughness (n = 5). The raw data was processed and imaged by the built-in software Vision 4.2.

2.5. *In vitro* antibacterial test

In vitro antibacterial test was conducted by *Staphylococcus aureus* (*S. aureus*, ATCC 25923) and *Escherichia coli* (*E. coli*, ATCC 25922). The bacteria were quantified and diluted to a concentration of 5 × 10^7 CFU/mL by the spread plate method. 500 μL bacterial solution was inoculated on the disc sample in a 37 °C incubator for 4 h 50 μL material co-cultured bacterial solution was then evenly spread on the AGAR plate, and incubated in a 37 °C incubator for 12 h. The number of colony-forming units (CFU) on the plate was observed and calculated accordingly. The same concentration and volume of bacterial solution were taken into the sterile cell culture plate, and the corresponding CFU was labeled as $CFU_{control}$. The CFU of the bacterial solution co-cultured with material was labeled as $CFU_{scaffold}$. The Inhibitive rate was calculated as follows: Inhibitive rate (%) = ($CFU_{control}$-$CFU_{scaffold}$)/$CFU_{control}$ × 100%.

2.6. Cell culture and *S. aureus* co-culture *in vitro*

The human umbilical vein endothelial cells (hVECs) and Raw264.7 cells were purchased from National Collection of Authenticated Cell Cultures. hVECs were cultured in endothelial cell medium (ECM, Science Cell) with 5 % FBS in a 37 °C thermostatic cell incubator containing 5 % CO_2 concentration. Raw264.7 cells were cultured in Dulbecco's Modified Eagle Medium (DMEM, Corning, USA) with 4500 mg/L glucose and 10 % FBS. In order to measure the effect of the material on the biological activity of the cells *in vitro*, the disc material was cleaned by 75 % ethanol and deionized water in sequence, sterilized and dried, and then soaked in ECM buffer or high glucose DMEM in a 37 °C incubator at the ratio of 200 mg/mL overnight, and the supernatant was extracted as the extraction solution for the next experimental step. 1 × 10^6/2.5 mL Raw264.7 cells and hVEC cells were implanted in 6-well plates and cultured in material extract for 5 days for the subsequent RNA extraction experiment. In addition, the disc sample was cleaned and sterilized according to the above steps, placed in a 48-well plate with an ultra-low adhesion surface, and then soaked in ECM buffer and left for 2 h in the cell incubator. After the culture solution was discarded,

20 μL suspension containing 2.5×10^5 hVECs was added on the scaffold for 2 h, and 500 μL ECM buffer was then added into each well.

In the bio-antibacterial test, 50 μL bacterial solution containing 5×10^5 CFU *S. aureus* was mixed with the cell suspension at the beginning for each well. The other steps of the corresponding bio-antibacterial test remained the same as the pure cell culture *in vitro*.

2.7. Cellular viability test

hVECs were digested by 0.25 % Trypsin-EDTA (Gibco) and counted with cell counting plates, diluted into 5×10^4/mL, then added in 96-well plates successively (100 μL/well), and left for overnight until the cells were attached to the wall. The original ECM buffer was replaced with material extract. In the biological antibacterial experiment, the colony concentration in the corresponding cell-bacterial blend was 10^7 CFU/mL. To quantify cell activity, we used the Cell Counting Kit 8 (CCK8, Dojindo, Japan) assay. ECM containing 10 % CCK8 reagent was exchanged with the original supernatant at the time points of 1, 2, 3, 4 days of culture, incubated for 4 h avoiding from light, and the absorbance at OD 450 nm band was detected by Fluorescence microplate reader (Infinite F50, TECAN, Hombrechtikon) (n = 3).

2.8. Cell morphology detection

hVECs were cultured with materials with or without bacterial for 3 days. After biphasic fixation with 2 % glutaraldehyde and osmic acid, the cells were dehydrated with gradient concentration ethanol (50%, 70%, 80%, 90%, 95%, 100%), and critical point drying was adopted to avoid surface tension and preserve the fine structure of the cells. The samples were then observed under SEM scanning.

As for immunofluorescence morphologic analysis, the supernatant was discarded after culturing for 3 days, the scaffold was immersed in 4 % paraformaldehyde, the cells were fixed at room temperature for 10 min, the membrane breaking solution (0.5 % TrintonX-100 dissolved in PBS) was used to permeate the cells at room temperature for 5 min, the 100 nM FITC-phalloidin working solution was added to the plate and incubated for 30 min avoiding light. Incubated in 10 μg/μL DAPI solution for 3–5 min, the treated materials were then observed under confocal fluorescence microscope (Leica, Germany).

2.9. Real-time quantitative polymerase chain reaction (qPCR) analysis

The hVECs and Raw264.7 cells were cultured separately in material extract for 5 days before being used to harvest RNA through an EZ-press RNA purification kit (EZbioscience, Shanghai, China). The purified RNA was converted into detectable complementary DNA (cDNA) by a reverse transcription step using a PrimeScript RT reagent kit (Takara, Dalian, China). The expression of angiogenesis related genes (vascular endothelial growth factor (VEGF) and basic fibroblast growth factor (bFGF)) and inflammatory cytokine (interleukin 6 (IL6), interleukin 1b (IL1b))-related genes (Table S2; Supporting Information (SI)) were detected on a PCR system (Bio-Rad, Hercules, CA, USA).

2.10. Subcutaneous back embedding of scaffolds in vivo

In order to observe the *in vivo* antibacterial response, vessel ingrowth and implant degradation under conventional bacteria-free conditions, the cylindrical scaffolds (Ø 10 × 5 mm) were used in the subcutaneous dorsal embedding experiment. The animal experiments were carried out under the approval of the Animal Ethics Committee of the Second Hospital of Zhejiang University (2018–333). Twelve 6-week-old female New Zealand white rabbits (2.5–3.0 Kg) were ordered from the Zhejiang University Laboratory Animal Center for subcutaneous back embedding. All materials are cleaned with 75 % ethanol and sterilized by high temperature and pressure steam prior to application. First, under the anesthesia of 3 % pentobarbital sodium, the skin and subcutaneous fascia of the back of rabbits were separated layer by layer under sterile conditions. In the sterile treatment group (n = 3), the materials were implanted into the subcutaneous tissue of the back and then sutured layer by layer. In the bacteria-carrying experimental group (n = 3), the materials were soaked in 10^6 CFU/mL *S. aureus* solution for 3 h after disinfection, and then implanted into the back of rabbits after forming a stable bacterial biofilm [38].

A systemic angiographic method was used for subcutaneous back embedding prosthesis. As for the systemic angiography at 1 and 2 months after subcutaneous back embedding surgery, experimental rabbits were anesthetized with 5 % pentobarbital and fixed on the operating table. After the chest and abdomen were shaved, sterilized and exposed, the aorta and postcava were separated, the aorta was catheterized, and the proximal end was ligated. First, 5 mL high concentration heparin (160 μM/mL) was rapidly injected into aorta, and then 400 mL low-concentration heparin (2 μM/mL) was injected into the aorta at a low speed. The proximal end of postcava was ligated and the distal end fistulization was performed. After the infusion of heparinized saline, the blood vessels were washed with normal saline for half an hour, and the angiographic contrast agent Microfil (Flow Tech, MA, USA) was rapidly injected. The rabbit carcass was stored at −20 °C overnight, the samples were taken at the next day and fixed with 4% paraformaldehyde. Excess soft tissue was removed after dehydration with gradient concentration ethanol. Micro-computerized tomography scanning (micro-CT, vivaCT100, Scanco Medical, Zurich, Switzerland) was employed to scan the samples and the built-in software was used for layer analysis and reconstruction to detect the surface area and volume of the new blood vessels.

In the experimental group with bacteria loading, samples were taken 2 weeks after implantation for H&E staining and Giemsa staining to observe the inflammatory response and colony growth.

2.11. Rabbit enucleation and prosthesis implantation

Seventy-two adult female New Zealand white rabbits (2.5–3.0 Kg) were used for enucleation and prosthesis implantation surgery of the right eye. Commercial and clinical HA and Medpor prostheses were used as controls in this study. After anesthetizing the rabbit through the ear vein, we further retrobulbar anesthetized it with 5 % pentobarbital sodium. We made a circular incision in the corneal limbus of rabbits to cut the conjunctiva, and separated four rectus muscles, and employed the figure of eight suture at the insertion point of the rectus muscle. The retrobulbar neurovascular bundle was closed with vascular clamp and clipped with ophthalmic nerve scissor, then the eyeball was eviscerated. Gauze was used to fill in the eye socket to stop bleeding. After the prosthesis was implanted, the broken ends of the rectus lateralis and rectus medialis were sutured, the broken ends of the superior and inferior rectus muscles were also sutured together and wound in a cross shape, Tenon's capsule and conjunctiva were sutured in layers, and pressure bandaging was performed. Experimental rabbits with prosthetic seat filling after enucleation were randomly divided into two groups to participate in angiography and tissue sampling respectively.

An *in-situ* head-neck circulatory angiographic method was applied for local head and neck angiography. Rabbits were anesthetized with 5% pentobarbital 1 and 2 months after enucleation and prothesis implantation for the head-neck circulatory angiography. Then they were shaved and disinfected on the chest, face and neck, and cut layer by layer, exposing the jugular vein and carotid artery. Carotid artery was catheterized, proximal cardiac end was ligated, proximal cardiac end of carotid vein was also ligated, and 500 mL low-concentration heparinized saline (2 μM/mL) was quickly injected, followed with 500 mL saline, and then angiographic contrast agent was quickly injected. The rest of the procedure is the same as the systemic angiography above.

At the time points 1 month and 2 months after surgical implantation, rabbits were executed by injection of excess pentobarbital, samples were taken, the prosthesis and its surrounding tissues were isolated, fixed in

4% paraformaldehyde for 1 week, dehydrated with gradient concentration ethanol, and then embedded in PMMA resin for 1 month. After hardening, the sample was cut along the central plane to a thickness of 100–200 μm and stained with H&E. The sections were observed by optical microscope (DMLA, Leica, Germany).

2.12. Statistical analysis

All data were expressed as mean ± standard deviation (SD), unpaired T-test and one-way ANOVA analysis were conducted by SPSS19.0 software (SPSS, Chicago, IL, USA). $P < 0.05$ indicated that the value had statistical difference and the result was statistically significant.

3. Results

3.1. Physicochemical characteristics of CSi-Znx samples

XRD analysis confirmed that the bioceramic powders with different Zn doping ratio were consistent with the phase crystalline β-wollastonite (PDF #27–0088; Fig. S1; SI). According to the ICP analysis, the Zn content in the three groups of CSi-Zn*x* bioceramic powders was 4.39 %, 8.51 %, and 13.45 %, respectively (Table S1; SI), which were close to the theoretical data before synthesis (4.5%, 9.0%, 13.5%).

The mechanical properties were evaluated by compression resistance test. As shown in Fig. 1A, the compressive strength of CSi-Zn*x* scaffolds were changed with increase of sintering temperatures (1050°C-1250 °C). In particular, the Zn-doped CSi porous samples sintering at 1150 °C exhibited highest compression resistance (50–70 MPa), and then showed a significant strength decay (<30 MPa) at 1250°C. The stress-strain curves also indicated the pure CSi scaffolds easily occurred a structural collapse than the Zn-doped CSi scaffolds. However, the porous structure maintained stably within 15 % strain during compression test for the Zn-containing scaffolds (Fig. 1B). Moreover, it was worth mentioned that the changes of elastic modulus of porous scaffolds were also similar to the trend of compressive strength (Fig. 1C).

SEM observation for the surface microstructures of as-sintered and buffer immersed samples was used to evaluate the bio-dissolution of CSi-Zn*x* samples (Fig. 2). Obviously, the increase of Zn content in CSi could enhance the sintering property and produce more dense microstructures and grain growth on the surface layer (Fig. 2A). On the other hand, it was worth noting that the pH value was increased for the pure CSi samples during immersion in Tris buffer, but this data was increased firstly and followed by a significant decrease in the CSi-Zn*x* groups (Fig. 2B). Meanwhile, the pure CSi samples also showed a remarkable mass loss (~12%) with increasing immersion time up to 6 weeks, while the increase of Zn dopant in CSi would result in significant inhibition of bio-dissolution in Tris buffer; the CSi–Zn9 and CSi–Zn13.5 bioceramic discs produced only 1.0%–1.5% mass loss after 6 weeks of immersion (Fig. 2C). Moreover, it was found from the Zn ion release curves that the doped Zn ions did may release into the aqueous medium, but its accumulative concentration (0.09–0.18 ppm) was very limited in the CSi–Zn9 and CSi–Zn13.5 groups (Fig. 2D). As expected, it was showed that the Ca and Si ion concentrations (<2 ppm) were inhibited significantly with increasing the Zn dopant (Fig. 2E and F). In contrast, the pure CSi could release appreciable Ca and Si ions in the buffer (>10 ppm).

3.2. In vitro cell viability and antibacterial potential of CSi-Znx bioceramics

In order to evaluate the antibacterial potential of sparingly dissolvable CSi-Zn*x* bioceramic, the representative gram-negative and gram-positive bacteria (e.g. *E. coli* and *S. aureus*) suspensions were spread on the AGAR plate after infiltrated with the CSi-Zn*x* scaffold for 4 h at a concentrate of 5×10^7 CFU/mL. It was obvious that the antibacterial potential was increased with increasing Zn content in the bioceramic, especially a stronger *S. aurecakeus*-killing effect in the CSi–Zn9 and CSi–Zn13.5 groups (Fig. S2; SI). Indeed, the inhibition rate of *E. coli* was limited (<50%), which showed inefficient antibacterial response in comparison with the National Standard (WST650-2019). On the other hand, according to the (co-)culture of hVECs in the bioceramic extract with and without *S. aureus* was carried out *in vitro* (Fig. S3A; SI), it was confirmed that the CSi–Zn9 and CSi–Zn13.5 could promote hVECs' proliferation in comparison with the pure CSi (Fig. S3B; SI), and interestingly this difference became apparent in the presence of *S. aureus* (Fig. S3C; SI).

In order to explore the direct antibacterial activity and cellular viability on the bioceramics, the SEM and immunofluorescence observation were performed. Fig. 3 showed that the hVECs exhibited similar morphology on the scaffolds, accompanying with extensive extension of filamentous and lamellar pseudopodia, similar number of cytoskeleton and nucleus (Fig. 3A). However, when *S. aureus* was co-existed in the culture system (simulating bacterial contamination), the cellular morphology was obviously damaged in the two low-Zn bioceramic groups, in which the numbers of living cells were significantly reduced (Fig. 3B).

As for the *in vivo* antibacterial potential and anti-inflammatory behavior of the bioceramics after injection of the bacterial solution, H&E staining results showed that there was no obvious tissue growth in the pure CSi pores, and the fibrous tissue growth was rare and sparsely distributed in the CSi–Zn4.5 scaffolds; in contrast, a large amount of fibrous tissue grew into the macropores of CSi–Zn9 and CSi–Zn13.5 scaffolds (Fig. 4A). The Giemsa staining showed that there were still residual colonies at the edges of CSi and CSi–Zn4.5 scaffolds, and the surrounding fiber tissue was exiguous. Nevertheless, the CSi–Zn9 and CSi–Zn13.5 groups showed fibrous tissue ingrowth in the center zone, without observing residual bacterial colonies (Fig. 4B).

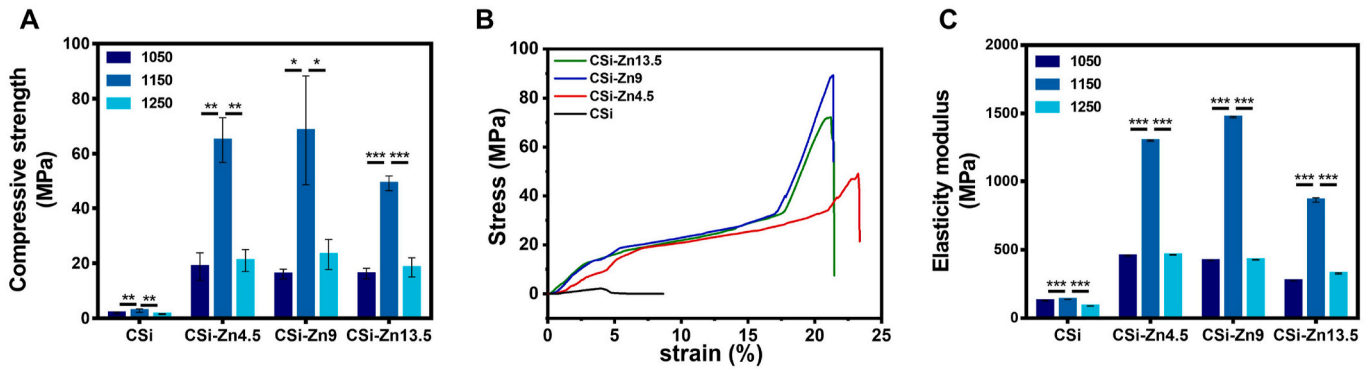

Fig. 1. Mechanical evaluation of CSi-Zn*x* scaffolds sintered at different temperatures (n = 3). (A) Compressive strength of porous CSi-Zn*x* samples. (B) Stress-strain curves of porous scaffolds. (C) Elasticity modulus of porous bioceramic samples. (*P < 0.05, **P < 0.005 , ***P < 0.0005).

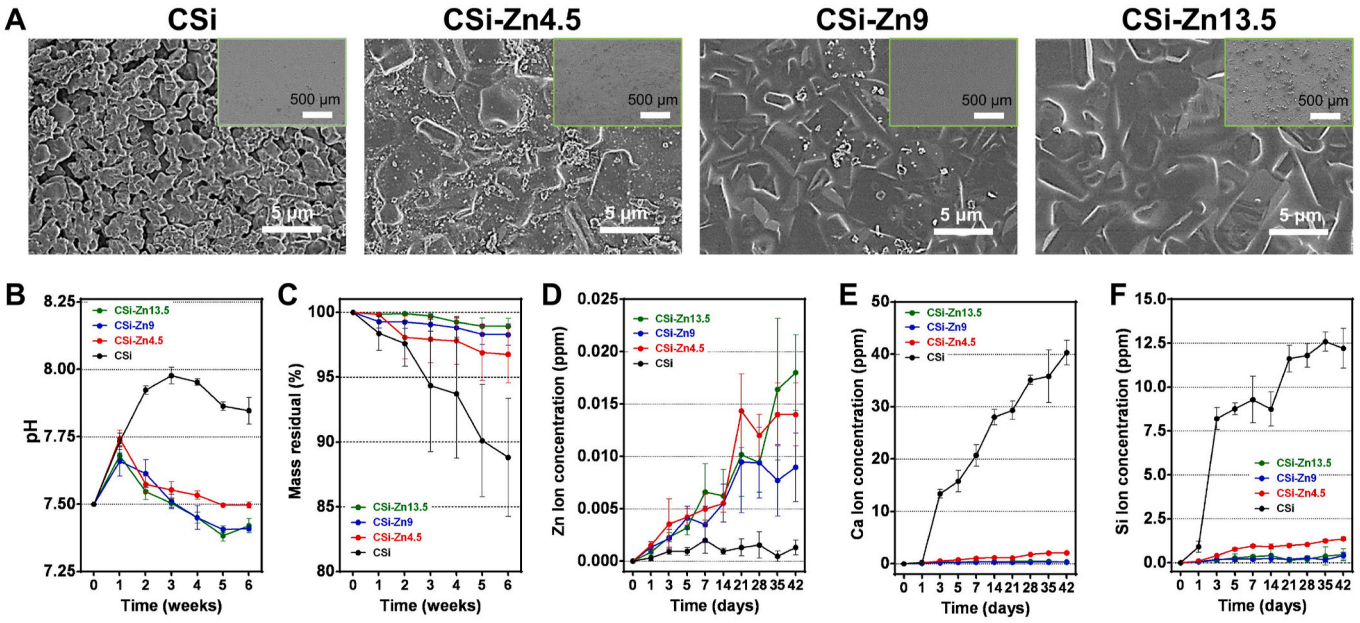

Fig. 2. Surface observation and Tris buffer immersion evaluation of CSi-Zn*x* discs. (A) The SEM image of CSi-Zn*x* discs. (B) Changes in pH value in Tris buffer. (C) Mass decay of bioceramic discs in Tris buffer. (D–F) Zn, Ca, and Si concentrations in Tris buffer n = 3. (*P < 0.05, **P < 0.005 , ***P < 0.0005).

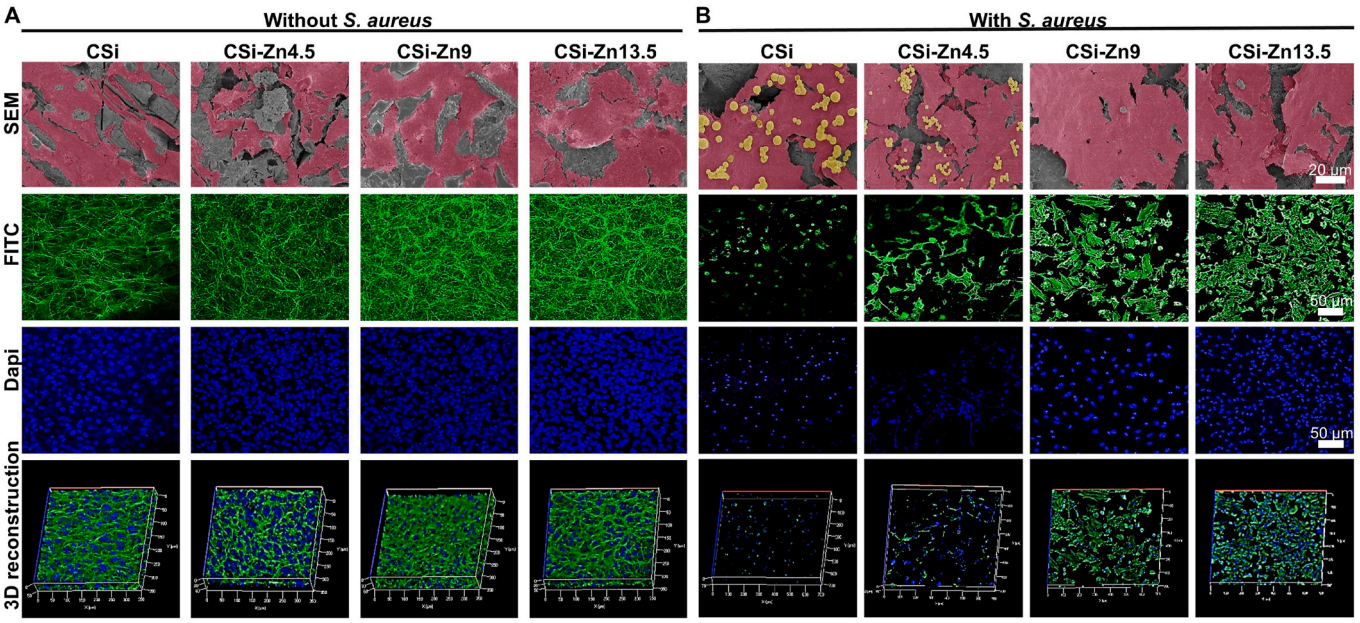

Fig. 3. SEM observation and FITC/Dapi immunofluorescence staining results of scaffold cocultured hVECs without and with *S. aureus*. (A) SEM images and FITC/Dapi immunofluorescence staining results of co-cultured hVECs/scaffold group. (B) SEM images and FITC/Dapi immunofluorescence staining results of co-cultured hVECs/*S. aureus*/scaffold co-culture group. From top to bottom are: SEM images of scaffold surface in the presence of hVECs (red) and S. aureus (yellow); Cytoskeleton labeled with FITC (green); Cell nucleus labeled with Dapi (blue); 3D reconstruction of merge images.

3.3. Angiogenic effect and biodegradation of CSi-Znx scaffolds

Fig. 5A showed the procedure of constructing cell seeding *in vitro* and subcutaneous dorsal embedding model *in vivo*. The quantitative PCR results revealed that the CSi-Zn*x* scaffolds outperformed the CSi group up to 7–20 times in VEGF expression (Figs. 5B) and 2–4.5 times in bFGF expression (Fig. 5C). Gene expression of inflammation related marker IL6 (Fig. 5D) and IL1b (Fig. 5E) mRNAs in Raw264.7 cells was significantly higher in the CSi–Zn9 groups. Angiogenesis images *in vivo* further showed that the remarkable neovascularization area (red-marking) was observed in the CSi–Zn9 and CSi–Zn13.5 groups at month 1 and 2 after implanting (Fig. 5F and G). The quantitative data also verified both CSi–Zn9 and CSi–Zn13.5 groups showed significant increase in neovascularization area and volume after one month (Fig. 5H and I), and meanwhile the CSi–Zn9 group still maintained its long-term angiogenesis dominance after 2 months (Fig. 5J and K).

Micro CT measurement was employed to detect the *in vivo* biodegradation of bioceramic scaffolds after implanting for 2 months. It is schematically shown in Fig. 6A, all of porous scaffolds remained intact except for the pure CSi. As shown in Fig. 6B, there was no significant difference in porosity among the CSi-Zn*x* groups during biodegradation. However, the surface area and specific surface area (the ratio of surface

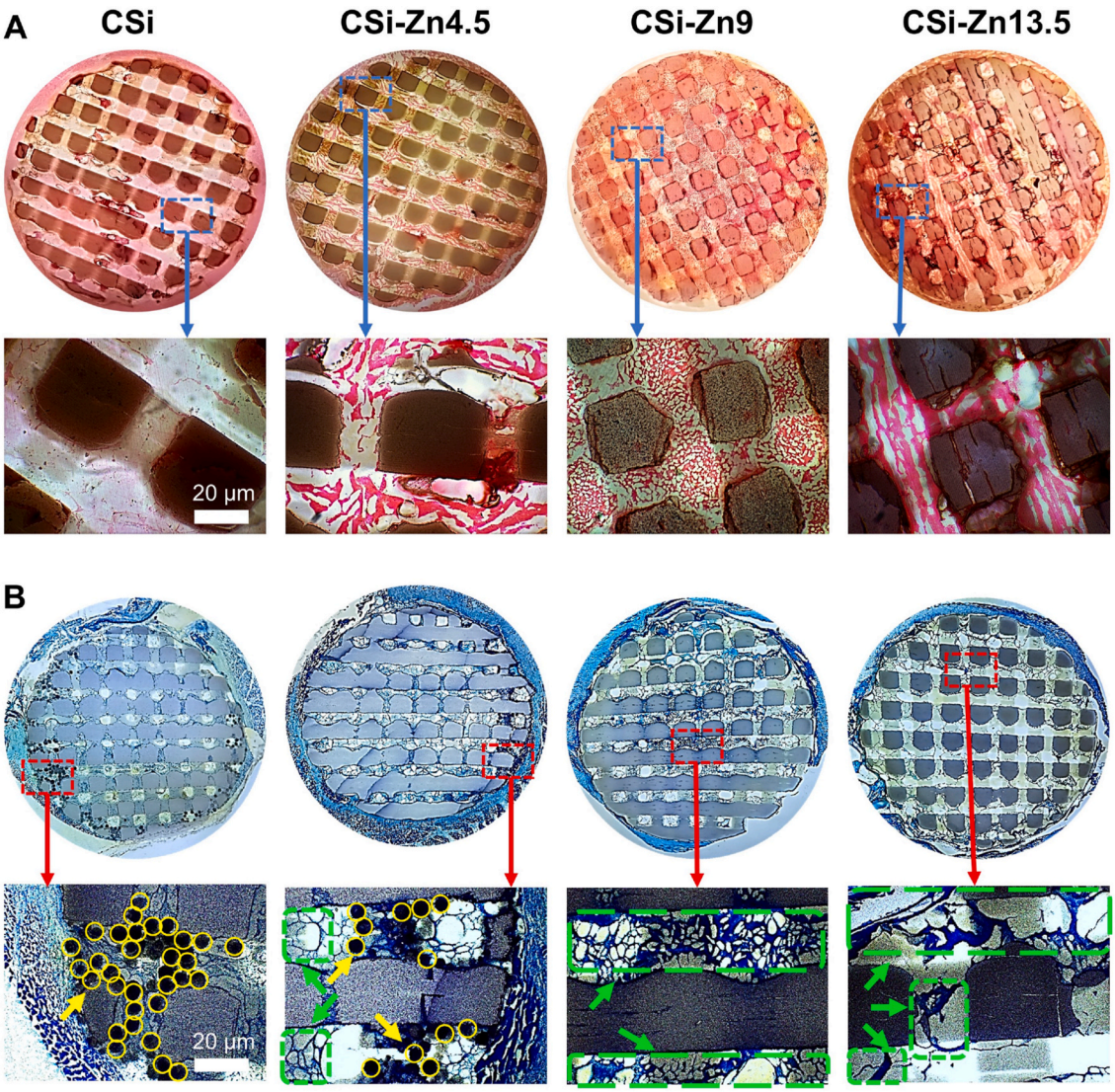

Fig. 4. H&E (A) and Giemsa (B) staining images of co-culturing hVECs/*S. aureus* on the CSi-Zn*x* scaffolds. Residual bacteria are marked with yellow arrows and circles, and fibrous tissue is marked with green arrows and dotted boxes.

area to volume) of CSi and CSi–Zn4.5 scaffolds were substantially higher than the other scaffolds (Fig. 6C and D), implying higher biodegradation of the two formers. Based on these experimental results, the CSi–Zn9 and CSi–Zn13.5 porous bioceramics were selected as orbital implants with skeleton-IWP or cubic pore geometries (i.e., Zn9-IWP, Zn9-Cubic, Zn13.5-IWP & Zn13.5-Cubic) to evaluate the orbital reconstruction.

3.4. Physicochemical characteristics of multiple orbital implant

As shown in Fig. 7A, the (fracture) surface microstructures of different morphologic apertures were observed by SEM. The radial pores in the 3D printed bioceramic spheres were unobstructed and regular in shape. Fig. 7B showed the surface roughness detection of 125 × 100 μm area of the spherical tip of all six scaffolds. As expected, the conventional HA scaffold had significantly different-sized pores on the surface layer, while the Medpor scaffold had very smooth surface. The surface roughness of CSi-Zn*x* scaffolds was between these two clinical products, which was consistent with the quantitative data (Fig. 7C). According to the microCT reconstruction (Fig. 7D), these scaffolds with IWP or cubic pores had fully interconnected micropores (200–400 μm), while the micropores in the clinically used HA implants were not completely interconnective. The quantitative analysis (Fig. 7E) indicated that the scaffold porosities were 40%–60% (HA 44–48%, Cubic 40–49%, IWP 52–60%). CFD permeability test results also showed that IWP model had higher permeability than cubic model (Fig. S9; SI). It was interesting that the IWP-pore CSi–Zn9 scaffolds exhibited appreciable surface area among all of groups, which was consistent with its theoretical structure.

The *in vitro* Tris buffer immersion test was employed to evaluate the bio-dissolution of the bioceramic scaffolds with different pore geometries. The micropore morphology and surface structures of scaffolds were not significantly different before and after immersion (Fig. 8A), implying the degree of *in vitro* bio-dissolution of CSi–Zn9 and CSi–Zn13.5 was very limited within the initial 4 weeks. Also, the mass loss and ion release behavior confirmed that such Zn-doped Ca-silicate porous bioceramic was sparingly dissolvable (<1.0 ppm) in a physiochemical pH condition (Fig. 8B–F), and indeed the Zn ion releasing dose was higher with increasing Zn dopant in the bioceramic. However, there was no significant difference between the scaffolds with different pore geometries. Moreover, the compressive modulus of the immersed scaffolds (Fig. 8G) showed a similar decay trend in comparison with the samples before immersion treatment.

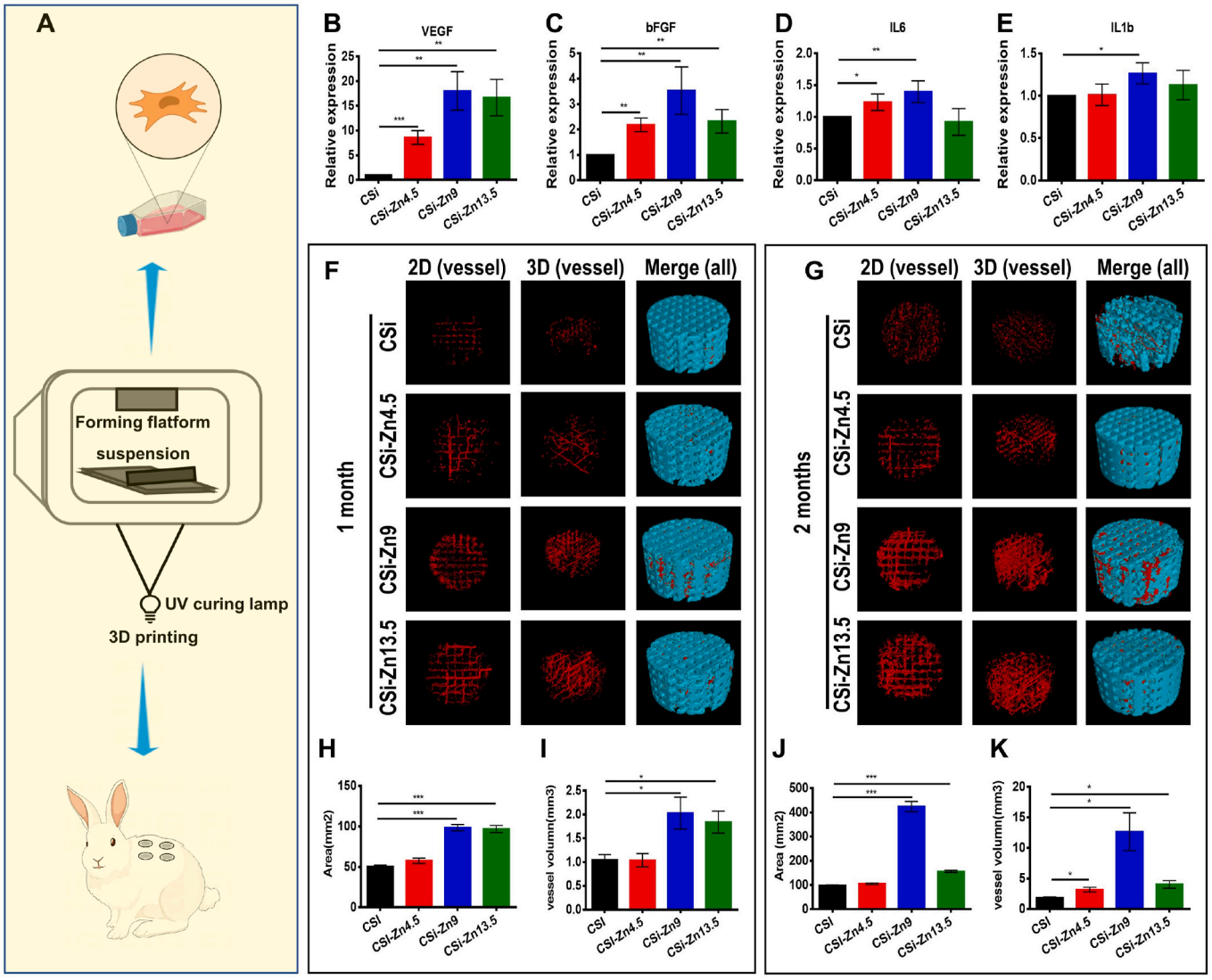

Fig. 5. Angiogenesis analysis *in vitro* and the detection of ectopic back embedding *in vivo*. (A) Scheme of angiogenesis detection *in vitro* and *in vivo*. (B–E) Angiogenic gene (VEGF, bFGF) and inflammation related gene (IL6, IL1b) detection *in vitro*. Neovascularization test at month 1 (F) and month 2 (G) after implantation and the related quantitative analysis (H–K). (*P < 0.05, **P < 0.005 , ***P < 0.0005).

3.5. Evaluation of biological reconstruction of orbital implant in vivo

Fig. 9A showed a representative schematic diagram of enucleation and implantation surgery. The angiography was used to detect the ingrowth of new blood vessels in prosthesis. After one month (Fig. 9B), the number of new blood vessels in all groups was limited, except for the Zn9-IWP group. With the prolongation of implantation time (2 months; Fig. 9C), the blood vessel density in all of new bioceramic groups was increased distinctly, and the Zn9-IWP group was the most densely distributed and consistent with the quantitative data (Fig. 9C and D). Indeed, it was worthy noted that the Medpor group showed limited vascularization within 2 months, in contrast with that in the Zn9-IWP group.

Moreover, the H&E stained sections were used to further detect the blood vessel ingrowth. As shown in Fig. 10, there was few neovasculation and tissue ingrowth in the HA group at one month and some fiber tissue could be observed in the Medpor group. Whereas new blood capillary was found in the 3D printed bioceramic groups, and more blood vessels may be observed in the Zn9-IWP group. After two months, plenty of soft tissue and newly grew blood vessels was observed in all groups; the micropores in the Zn9-IWP scaffolds were almost filled with vascular tissue. Also, the thicker blood vessels were observed in the Medpor, Zn9-Cubic and Zn13.5-IWP groups, whereas the micropores of HA and Zn13.5-Cubic scaffolds were almost dominated by new soft tissue fibers.

4. Discussion

It is well agreed that an ideal orbital implant should have some critical features such as suitable filling volume, good transfer ability of fixed orbital implant to exterior wearable prosthesis, adequate mechanical support, low complication rate, and non-biodegradable. However, some problems including displacement, extrusion, postoperative infection and poor mobility are still difficultly overcome in orbital prothesis nowadays [39,40]. Hence, the newly developing biomaterials with appreciable antibacterial effects and vasculogenic ability are being expected to conquer the clinical applications.

As a clinical implant, prosthetic eye is required to high biological stability (low biodegradation) and high biocompatibility, which are favorable for long-term maintaining orbital volume and interactive mobility in eye socket. As we know, the pure CSi bioceramic has been demonstrated to be high biodegradability and low mechanical strength,

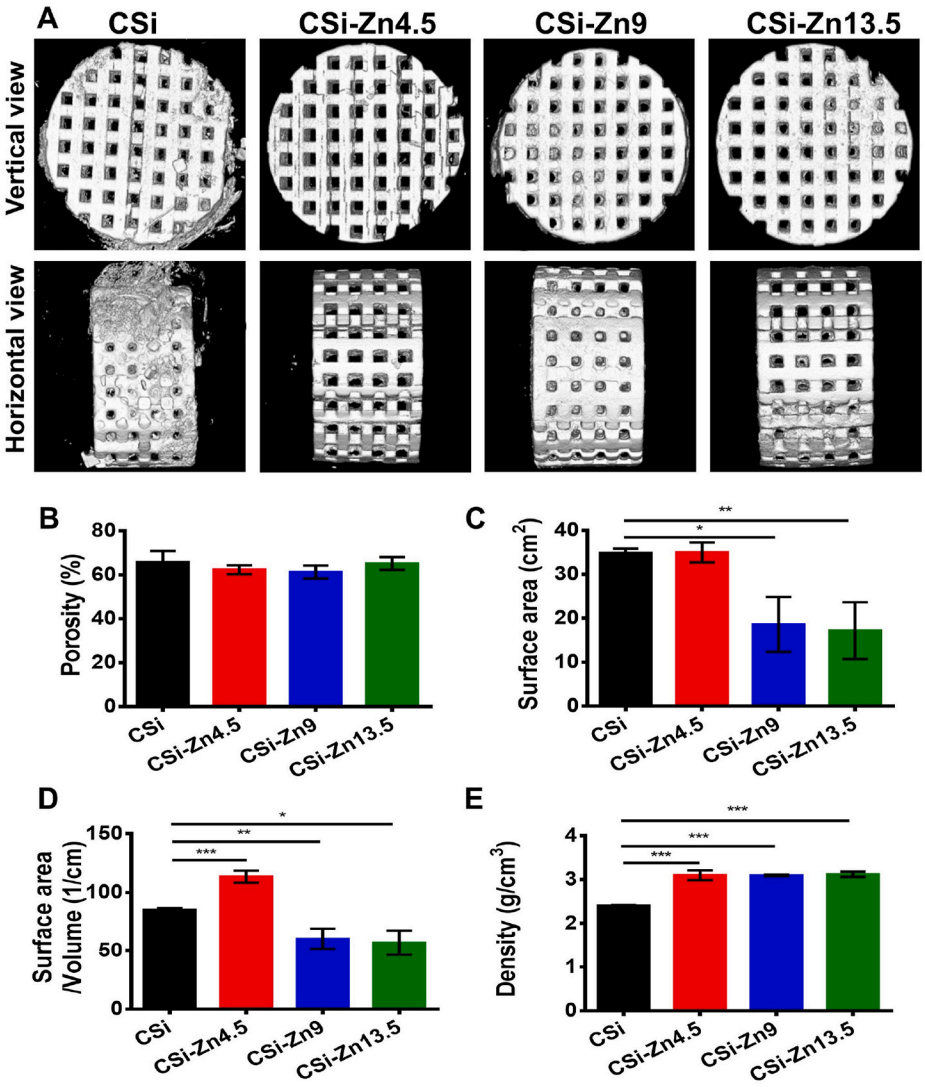

Fig. 6. Morphological characterization and quantitative analysis of biodegradation of bioceeamic scaffolds after 2 months *in vivo*. (A) μCT reconstruction of the 3D bioceramic scaffolds. (B) Porosity of bioceramic scaffolds. (C) Surface area of bioceramic scaffolds. (D) Surface area/volume of bioceramic scaffolds. (E) Density quantitative analysis of bioceramic scaffolds. (*P < 0.05, **P < 0.005 , ***P < 0.0005).

and these properties are disadvantageous as orbital implant application. It is interesting that, however, the presence of zinc in a typical Ca-silicate ceramics (i.e. hardystonite; Ca_2ZnSiO_7) exhibit significantly low biodegradation *in vitro*, but may increase cellular proliferation and differentiation compared to CSi [41]. Accordingly, it is reasonable to assume that low dosage of Zn ion selective doping would be helpful for tuning the biodegradation property of CSi and meanwhile maintaining its high biological activity. In this aspect, the previous studies have shown that zinc-doped CSi can act as a coating biomaterial to promote the proliferation and differentiation of bone marrow-derived pericytes, and even improve the bone integration with the alloy implants [24]. Salvatore's and co-workers also indicated that Zn-modified CSi bioceramics may promote osteogenic differentiation *in vitro* [42]. In this study, we attempted to optimize the customizable porous orbital implants via Zn doping in CSi and 3D printing technique. The CSi-Zn*x* scaffolds exhibited different bio-dissolution rates and ion release behavior *in vitro* according to different Zn contents. It is worth mentioning that the 13.5% Zn substituting CSi still retained the β-wollastonite phase (Fig. S1; SI), and the sintering property was significantly enhanced after treatment at 1150°C (Figs. 1 & 2A). And it is evident that the Ca and Si release was heavily inhibited with increasing Zn dopant in comparison with the pure CSi (Fig. 2E and F). Moreover, the presence of Zn in CSi bioceramic could be favorable for stabilizing the pH value in the buffer medium (Fig. 2B). Previous studies have shown that the incorporation of zinc can effectively reduce the potential pH-dependent cell damage [43]. Therefore, appropriate amount of Zn dopant in CSi could be valuable to study systematically as the new orbital implants.

In general, postoperative infection is a severe complication in the clinic. The conventional clinical material disinfection, exogenous antibiotic adsorption and postoperative antibiotic injection may not completely overcome the occurrence of infection. Meanwhile, the conventional prosthetic eye candidates often rely on the insertion of titanium nails to enhance coupling activity, which is often a source of postoperative infection [44]. Therefore, antimicrobial property is one of the main limitations of current prosthetic eye materials [40,45]. In this aspect, our study indicated that with the increase of zinc dopant, the antibacterial potential of CSi-Zn*x* against the common bacterial in exophthalmic infection (*S. aureus*) [46,47] was increased gradually (Fig. S2; SI). It was abnormal but expected that in the cell/bacteria co-culture experiment, the CSi–Zn9 and CSi–Zn13.5 groups exhibited appreciable antibacterial effect and meanwhile had no adverse effects on the morphology and quantity of hVECs (Fig. 3). These results indicate that the CSi–Zn9 and CSi–Zn13.5 possess excellent contact-active

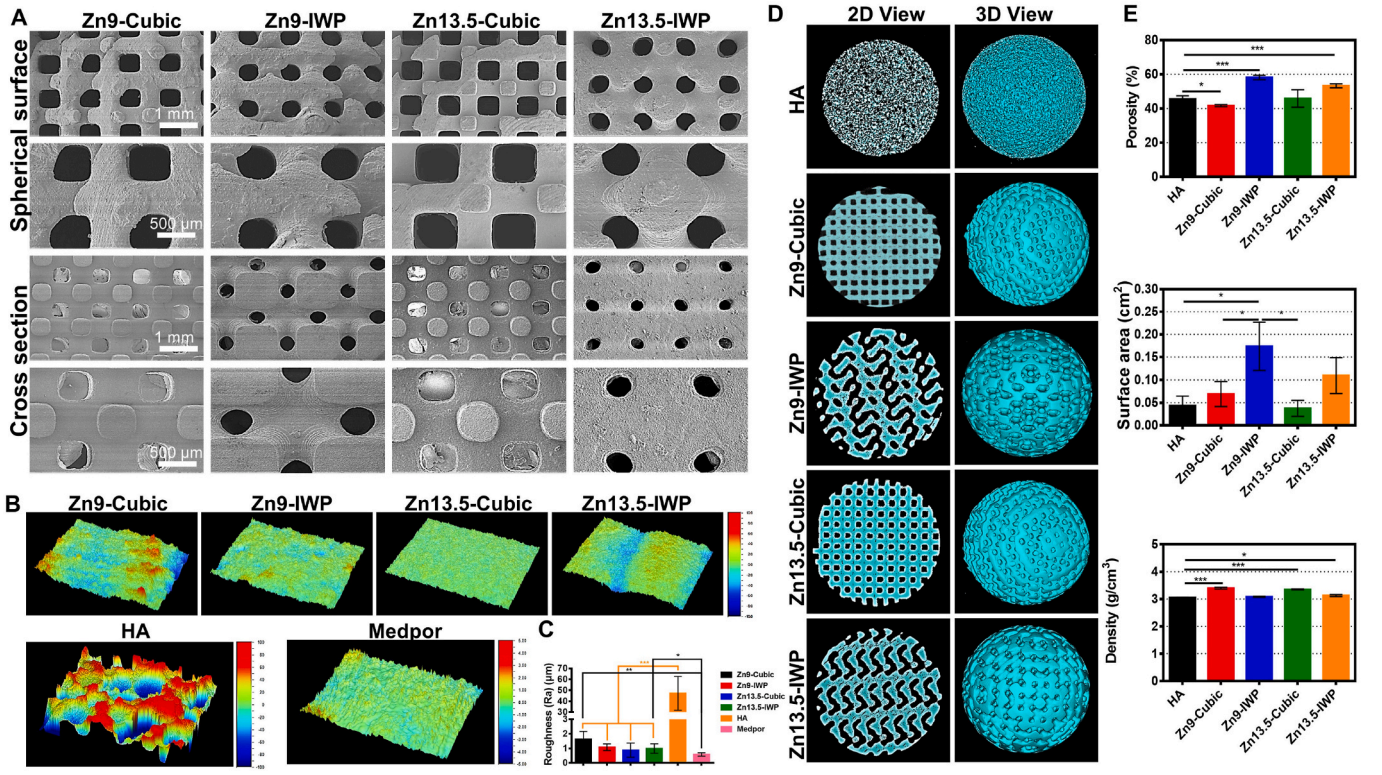

Fig. 7. Surface morphological characterization and quantitative analysis detection results of orbital implants. (A) SEM images of spherical surface and cross section views of Zn9-Cubic, Zn9-IWP, Zn13.5-Cubic, Zn13.5-IWP scaffolds. (B) Surface roughness detection of Zn9-Cubic, Zn9-IWP, Zn13.5-Cubic, Zn13.5-IWP, HA, Medpor scaffolds. (C) Quantitative analysis of surface roughness detection. (D) Micro-CT 2D and 3D reconstruction views of HA, Zn9-Cubic, Zn9-IWP, Zn13.5-Cubic, Zn13.5-IWP scaffolds. (E) Porosity, surface area and density quantitative analysis of scaffolds. (*P < 0.05, **P < 0.005, ***P < 0.0005).

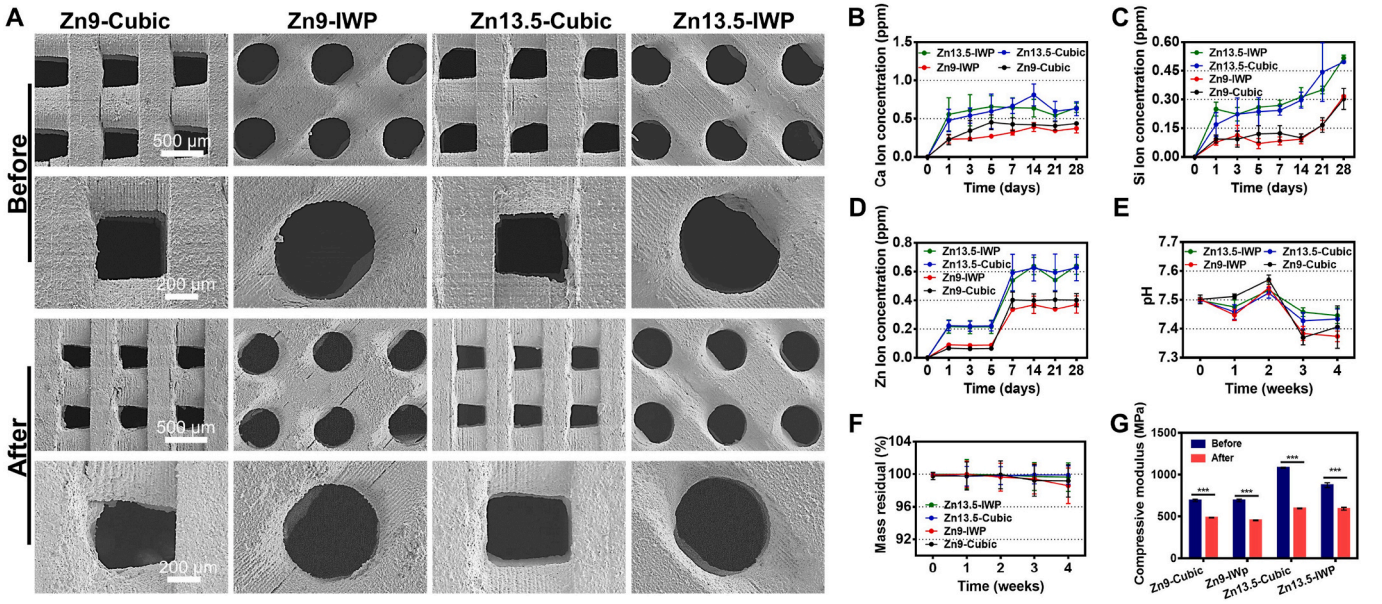

Fig. 8. In vitro degradation experiment and analysis of spherical and cylindrical scaffolds. (A) SEM images of Zn9-Cubic, Zn9-IWP, Zn13.5-Cubic, Zn13.5-IWP cylindrical scaffolds before and after *in vitro* degradation test. (B–F) Ca, Si, Zn concentration, pH change, and mass loss of spherical scaffolds in Tris buffer in 4 weeks, n = 3. (G) Compressive modulus analysis of the cylindrical scaffolds before and after degradation *in vitro*. (*P < 0.05, **P < 0.005, ***P < 0.0005).

antibacterial potential, similar to the Ca–Mg-silicate bioceramics in our previous study [46,47]. In fact, the potent antibacterial capability evaluated *in vivo* also suggested that *S. aureus* could not endure the CSi–Zn9 and CSi–Zn13.5 bioceramics in the early stage (Fig. 4).

On the other hand, vascularization is an important criterion for evaluating the histocompatibility of surrounding tissue of porous orbital implants. Our previous studies had shown that Ca-silicate bioceramics have a significant effect on early angiogenesis *in vivo* in panniculus carnosus muscle model [48,49]. Meanwhile, it is reported that zinc can significantly promote angiogenesis during cerebral ischemic repair by

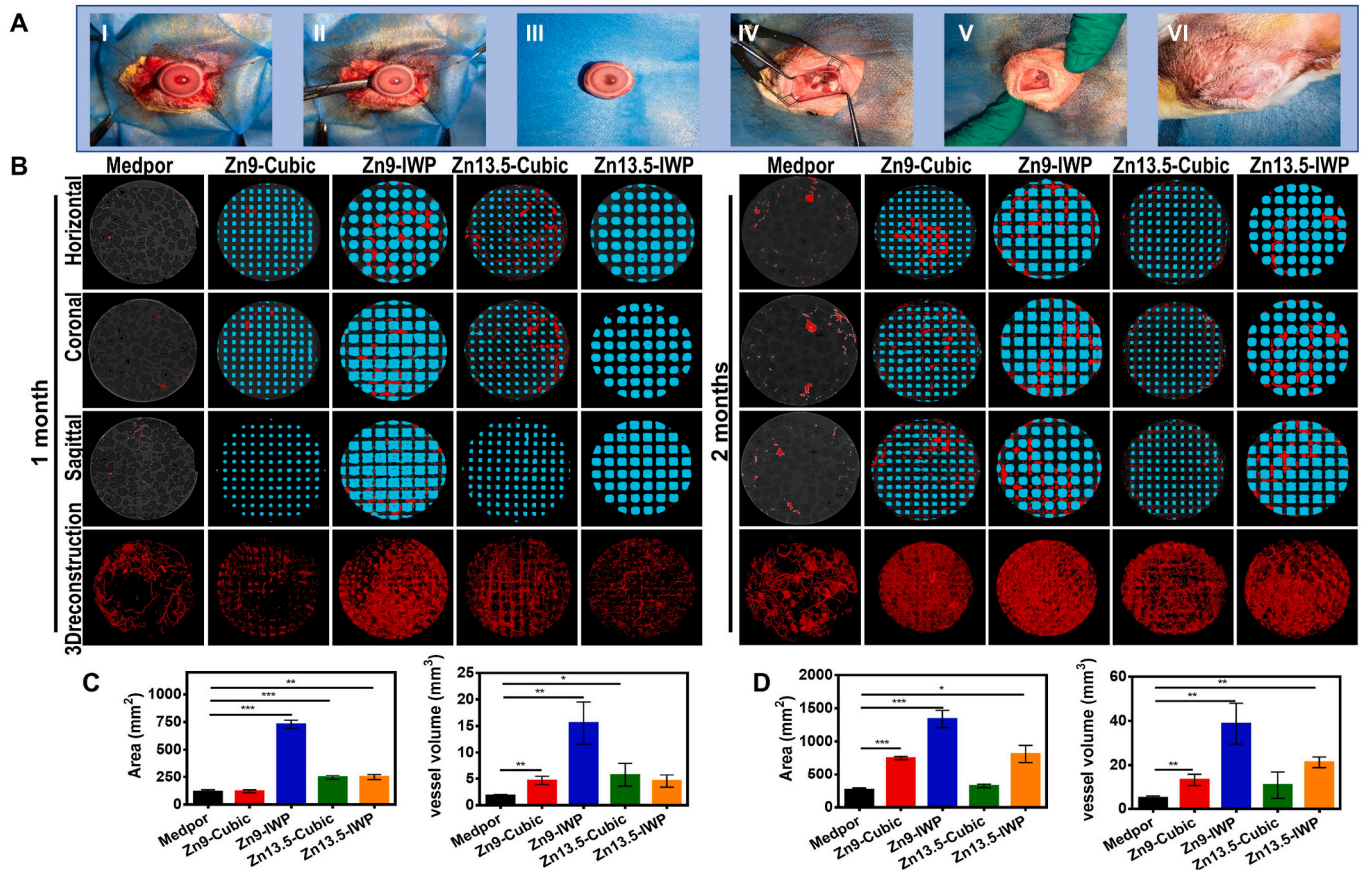

Fig. 9. Schematic diagram of the procedure for enucleation and the images of live angiogram. (A) Schematic diagram of the procedure for enucleation, (B) Angiographic reconstruction images of the orbital implants and internal blood vessels after 1 and 2 months, respectively. Among them, due to the undevelopable property of Medpor scaffold in microCT, there was no associated scaffold image. Since the density parameters of HA scaffold were similar to intravascular contrast medium, angiography could not distinguish the difference between the two, so there was no relevant result. (C) Quantitative analysis of total vascular area and total volume in angiography 1 month after implantation. (D) Quantitative analysis of total vascular area and total volume in angiography 2 months after implantation. (*P < 0.05, **P < 0.005, ***P < 0.0005).

increasing the levels of VEGF-A and VEGF-R2 proteins in astrocytes [50]. As for potential vascular differentiational functional ions, our experiments also confirm that the CSi-Zn*x* significantly promote the up-regulation of vasculogenesis related genes (VEGF and bFGF) compared with pure CSi. Other study have showed that zinc-doped bioceramic scaffold could activate the p38 signaling pathway by regulating monocytes and build a microenvironment conducive to the formation of blood vessels [51]. It is known that Zn and Si can cooperate to induce the recruitment, biological activity and differentiation ability of hair follicle cells, and even promote wound healing [52,53]. Hence, Zn dopant have acted as a bifunctional ion in CSi which is beneficial for next-generation orbital implant development.

Angiogenesis efficiency is also closely related to pore morphology and structural parameters. The pore size, porosity, surface area and roughness of porous scaffolds have been proved to be critical for newly formed tissue ingrowth. In the present study, it was showed that the curved micropores had better angiogenesis effect, which was revealed by the difference in the Zn9-IWP and Zn13.5-IWP groups (Fig. 9C and D). These results agree well with the existing studies on biomaterial with high porosity of more than 80%, which allows more cells and nutrients migration into the implants, and thus promotes tissue ingrowth [54]. Interestingly, the Zn9-IWP scaffolds have more appreciable surface area (~0.18 mm^2) and porosity (~60 %; Fig. 7E). Some studies also suggest that there is a positive correlation between total surface area of materials and tissue ingrowth, and it is speculated that a larger surface area allows more cell-implant interactions [55]. In general, it is assume that the proper pore sizes should be greater than 150 μm, and preferably around 400 μm, which is helpful for promoting tissue ingrowth [56]. Also, another report shows that the proper pore size (100–400 μm) can contribute to the inward growth of tissues [57], which was consistent with the IWP-pore scaffolds with 200–400 μm and superior angiogenic performance. It is worthy mentioned that the surface roughness of prosthetic eye HA material is very high (~45 μm), and this factor would also contribute on the tissue damage through the interaction between the material and the wrapped tissue. In our surgery, the clinically used HA implants are difficult to be successfully placed at one time, and the embedding process is resisted. In contrast, the surface roughness of CSi-Zn*x* scaffolds (0.4–1.8 μm) were very low, close to Medpor (0.4–0.8 μm; Fig. 7C), in which case reducing the intraoperative injury to conjunctiva.

Moreover, vascular reconstruction and rapid vascularization are both factors for the fusion of the prosthesis with the host, which allows the fibrous tissue ingrowth and fixing the implant, providing sufficient mobility, and also transport sufficient nutrients and immune cells through the blood vessels, avoiding the risk of postoperative infection [58]. In this study, angiography and quantitative analysis at 1–2 month after implantation revealed the superior of Zn9-IWP (Fig. 9C and D). In terms of fibrous tissue ingrowth, the fibro-vascularization of CSi-Zn*x* scaffolds reached 100% after 1 month, which was similar to the clinically available Medpor products. The Zn9-IWP and Zn13.5-IWP group had large aperture vessels with a diameter greater than 50 μm in 1 month after implantation. The rate of fibro-angiogenesis in Zn9-IWP group at 1 month was significantly higher than that in the HA group. Additionally, the ingrowth of surrounding tissue is affected by the

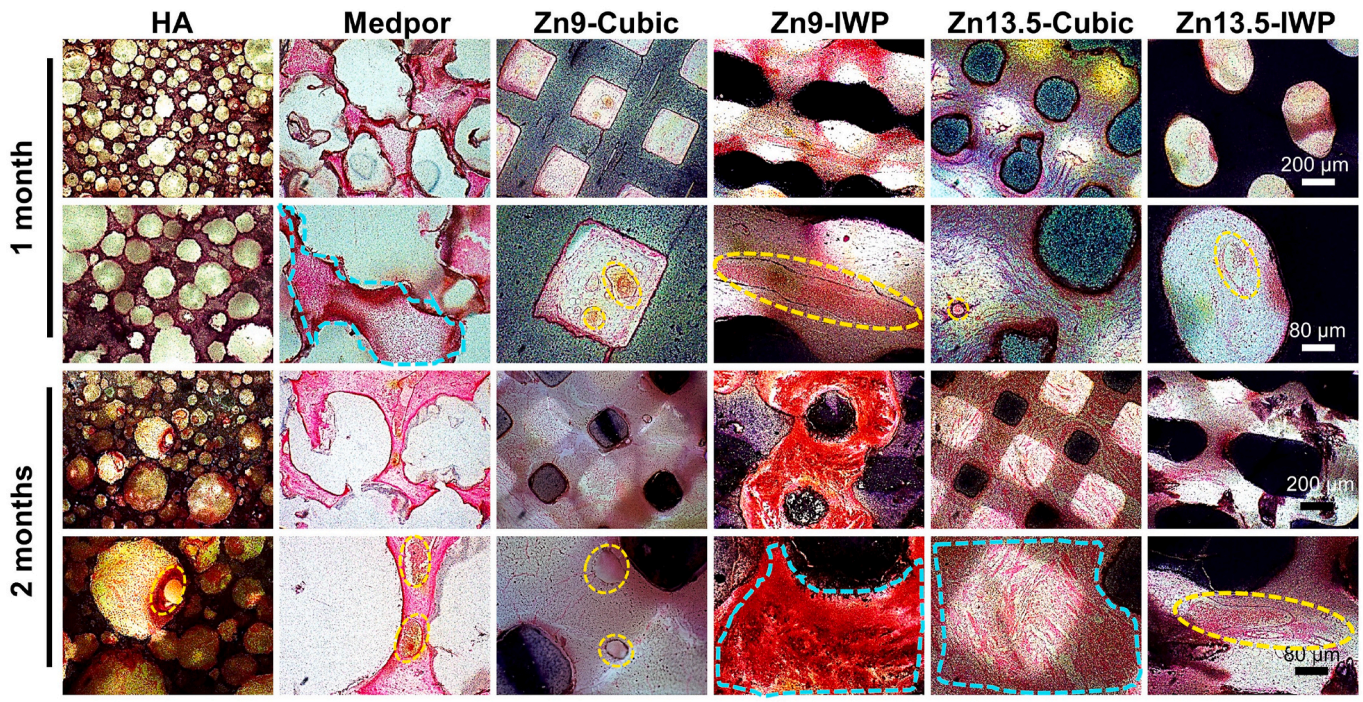

Fig. 10. Results of H&E staining sections of orbital implant materials and surrounding tissue 1 month and 2 months after enucleation and implantation surgery. The upper two lines of images are the results of staining 1 month after surgery, and the lower two lines of images are the results of staining 2 months after surgery. The first and third lines show the staining results of each group's sections under the low power microscope, and the second and fourth lines are the locally enlarged images of the previous row. In high power images, neovasculation is marked with yellow dotted circles, and large area of new fibrous tissue is marked with blue dotted circles.

dynamic interaction between the host environment and the orbital implant. The chemical composition, microstructure and mechanical support of the implants are helpful to maintain the prothesis fitting for the orbital volume. Based on these angiogenesis evaluations after implantation of prosthesis, it is reasonable to consider that the excellent angiogenic potential of Zn9-IWP scaffolds is related to its large specific surface area, and the ion release mediated by the curved pore surface play an important role in vascular induction response. The pore surface morphology can effectively induce interfacial blood vessels, and Zn ion release can accelerate the combination of the prosthesis implant with the primary socket environment by promoting early angiogenesis.

Totally, computer-aided design and 3D printing CSi-Zn*x* scaffolds can personalize and optimize the performance of Ca-silicate bioceramic implants. This technique can precisely regulate the apertural and outward morphology of the implant as well as the microscopic surface characteristic, and induce the growth of vascular tissue. However, further experiments are needed to explore the reasons for the vascular induction superiority of the 9% Zn-substituted CSi scaffolds with IWP pore geometry, which will help us to understand the material-tissue interface interaction and the effect of material apparent morphology on bioactivity, and ultimately be applied to the clinically translational implants in the near future.

5. Conclusion

In summary, the new selective ion doping porous bioceramic orbital implants with a finely tunable pore structure have been developed through computer-aided design and DLP technology. The physicochemical properties, antibacterial potential, and (ectopic) angiogenic performances were evaluated systematically. It is indicated that the IWP curved pore structure and 9% Zn dopant in CSi bioceramic could provide some advantageous structures and functions favorable for the antibacterial requirement and angiogenesis in orbital reconstruction. These findings indicate that the precise design of pore morphology and biologically functional inorganic ion doping may significantly enhance clinical applications of the conventional Ca-silicate bioceramic from orthopedic to orbital reconstruction area, and in particularly the newly developed Zn-doped CSi porous implants may overcome the well-known clinical difficulties in orbital prothesis.

Ethics approval and consent to participate

The animal experiments were carried out under the approval of the Animal Ethics Committee of the Second Hospital of Zhejiang University (2018–333).

CRediT authorship contribution statement

Yiyu Peng: Writing – review & editing, Writing – original draft, Visualization, Validation, Methodology, Investigation, Formal analysis, Data curation, Conceptualization. **Menglu Chen:** Investigation, Formal analysis, Data curation. **Jingyi Wang:** Data curation, Conceptualization. **Jiajun Xie:** Investigation, Funding acquisition. **Changjun Wang:** Methodology, Investigation, Funding acquisition. **Xianyan Yang:** Supervision, Software, Methodology, Funding acquisition. **Xiaoling Huang:** Visualization, Validation, Software. **Zhongru Gou:** Writing – review & editing, Visualization, Supervision, Resources, Funding acquisition, Conceptualization. **Juan Ye:** Writing – review & editing, Supervision.

Declaration of competing interest

The authors declare that they have no conflict of interests.

Acknowledgments

Authors would like to acknowledge financial support from the National Natural Science Foundation Regional Innovation and

Development Joint Fund (U20A20386), the Zhejiang Provincial Basic Research for Public Welfare Funds (LGF22E030002), National Natural Science Foundation of China (82330032, 82201236), and Zhejiang Provincial Natural Science Foundation of China (LZ22E020002).

Appendix A. Supplementary data

Supplementary data to this article can be found online at https://doi.org/10.1016/j.bioactmat.2024.02.027.

References

[1] G.G. Massry, B. Holds, Coralline hydroxyapatite spheres as secondary orbital implants in anophthalmos, Ophthalmology 102 (1995), 161-6.
[2] M.M. Sobti, F. Shams, L. Jawaheer, P. Cauchi, V. Chadha, Unwrapped hydroxyapatite orbital implants: our experience in 347 cases, Eye (London, England) 34 (2020) 675–682.
[3] M.N. Naik, R.K. Murthy, S.G. Honavar, Comparison of vascularization of Medpor and Medpor-Plus orbital implants: a prospective, randomized study, Ophthalmic Plast. Reconstr. Surg. 23 (2007) 463–467.
[4] S. Gradinaru, V. Popescu, C. Leasu, S. Pricopie, S. Yasin, R. Ciuluvica, et al., Hydroxyapatite ocular implant and non-integrated implants in eviscerated patients, J. Med. life 8 (2015) 90–93.
[5] S.G. Lee, J.W. Yang, S.G. Park, Y.I. Yang, Effect of stem cells and fibrin concentration on the vascularization of the Medpor orbital implant, Clin. Exp. Ophthalmol. 38 (2010) 885–891.
[6] R. Thiesmann, A. Anagnostopoulos, B. Stemplewitz, [Long-term results of the compatibility of a coralline hydroxyapatite implant as eye replacement], Ophthalmologe : Fortschritte Ophthalmol. Z. Dtsch. Ophthalmol. Ges. 115 (2018) 131–136.
[7] L.S. Han, R.B. Keillor, R.G. Weatherhead, Case series of shrinking hydroxyapatite orbital implants, Br. J. Ophthalmol. 105 (2021) 1338–1340.
[8] M. Cepela, S. Teske, Orbital implants, Curr. Opin. Ophthalmol. 7 (1996) 38–42.
[9] C. Edelstein, C.L. Shields, P. De Potter, J.A. Shields, Complications of motility peg placement for the hydroxyapatite orbital implant, Ophthalmology 104 (1997) 1616–1621.
[10] B. Zhang, X. Yin, Customized bioceramic scaffolds and metal meshes for challenging large-size mandibular bone defect regeneration and repair, Regen. Biomater. 10 (2023) rbad057.
[11] C. Qin, H. Zhang, L. Chen, M. Zhang, J. Ma, H. Zhuang, et al., Cell-Laden scaffolds for vascular-innervated bone regeneration, Adv. Healthcare Mater. 12 (2023) e2201923.
[12] E. Steijvers, A. Ghei, Z. Xia, Manufacturing artificial bone allografts: a perspective, Biomater. Transl. 3 (2022) 65–80.
[13] J. Yang, C. Deng, M. Shafiq, Z. Li, Q. Zhang, H. Du, et al., Localized delivery of FTY-720 from 3D printed cell-laden gelatin/silk fibroin composite scaffolds for enhanced vascularized bone regeneration, Smart Mater. Med. 3 (2022) 217–229.
[14] X. Yu, X. Wang, D. Li, R. Sheng, Y. Qian, R. Zhu, et al., Mechanically reinforced injectable bioactive nanocomposite hydrogels for in-situ bone regeneration, Chem. Eng. J. 433 (2022) 132799.
[15] F. Baino, C. Vitale-Brovarone, Bioceramics in ophthalmology, Acta Biomater. 10 (2014) 3372–3397.
[16] F. Baino, D. Falvo, Labate G. Urso, G.G. di Confiengo, M.G. Faga, C. Vitale-Brovarone, G. Catapano, Microstructural characterization and robust comparison of ceramic porous orbital implants, J. Eur. Ceram. Soc. 38 (2018) 2988–2993.
[17] R. Ge, C. Xun, J. Yang, W. Jia, Y. Li, In vivo therapeutic effect of wollastonite and hydroxyapatite on bone defect, Biomed. Mater. 14 (2019) 065013.
[18] C.G. Zenebe, A review on the role of wollastonite biomaterial in bone tissue engineering, BioMed Res. Int. 2022 (2022) 4996530.
[19] G. Qian, P. Fan, F. He, J. Ye, Novel strategy to accelerate bone regeneration of calcium phosphate cement by incorporating 3D plotted poly(lactic-co-glycolic acid) network and bioactive wollastonite, Adv. Healthcare Mater. 8 (2019) e1801325.
[20] D.U. Tulyaganov, K. Dimitriadis, S. Agathopoulos, F. Baino, H.R. Fernandes, Wollastonite-containing glass-ceramics from the CaO–Al2O3–SiO2 and CaO–MgO–SiO2 ternary systems, Open Ceram. 17 (2024) 100507.
[21] P. Zhou, D. Xia, Z. Ni, T. Ou, Y. Wang, H. Zhang, et al., Calcium silicate bioactive ceramics induce osteogenesis through oncostatin M, Bioact. Mater. 6 (2021) 810–822.
[22] S. Xu, K. Lin, Z. Wang, J. Chang, L. Wang, J. Lu, et al., Reconstruction of calvarial defect of rabbits using porous calcium silicate bioactive ceramics, Biomaterials 29 (2008) 2588–2596.
[23] Z. Fu, D. Li, J. Cui, H. Xu, C. Yuan, P. Wang, et al., Promoting bone regeneration via bioactive calcium silicate nanowires reinforced poly (ε-caprolactone) electrospun fibrous membranes, Mater. Des. 226 (2023) 111671.
[24] J. Yu, L. Xu, K. Li, N. Xie, Y. Xi, Y. Wang, et al., Zinc-modified calcium silicate coatings promote osteogenic differentiation through TGF-β/smad pathway and osseointegration in osteopenic rabbits, Sci. Rep. 7 (2017) 3440.
[25] A. Liu, M. Sun, H. Shao, X. Yang, C. Ma, D. He, et al., The outstanding mechanical response and bone regeneration capacity of robocast dilute magnesium-doped wollastonite scaffolds in critical size bone defects, J. Mater. Chem. B 4 (2016) 3945–3958.
[26] Y. Peng, J. Wang, X. Dai, M. Chen, Z. Bao, X. Yang, et al., Precisely tuning the pore-wall surface composition of bioceramic scaffolds facilitates angiogenesis and orbital bone defect repair, ACS Appl. Mater. Interfaces 14 (2022) 43987–44001.
[27] S. Azeena, N. Subhapradha, N. Selvamurugan, S. Narayan, N. Srinivasan, R. Murugesan, et al., Antibacterial activity of agricultural waste derived wollastonite doped with copper for bone tissue engineering, Mater. Sci. Eng., C 71 (2017) 1156–1165.
[28] Y. Hou, Y. Xia, Y. Pan, S. Tang, X. Sun, Y. Xie, et al., Influences of mesoporous zinc-calcium silicate on water absorption, degradability, antibacterial efficacy, hemostatic performances and cell viability to microporous starch based hemostat, Mater. Sci. Eng., C 76 (2017) 340–349.
[29] C. McClain, P. Morris, B. Hennig, Zinc and endothelial function, Nutrition 11 (1995) 117–120.
[30] S.A. Sreenivasamurthy, F.F. Akhter, A. Akhter, Y. Su, D. Zhu, Cellular mechanisms of biodegradable zinc and magnesium materials on promoting angiogenesis, Biomater. Adv. 139 (2022) 213023.
[31] F. Mendes Garrido Abregú, M.N. Gobetto, L.V. Juriol, C. Caniffi, R. Elesgaray, A. L. Tomat, et al., Developmental programming of vascular dysfunction by prenatal and postnatal zinc deficiency in male and female rats, J. Nutr. Biochem. 56 (2018) 89–98.
[32] M. Furko, Y. Jiang, T.A. Wilkins, C. Balázsi, Electrochemical and morphological investigation of silver and zinc modified calcium phosphate bioceramic coatings on metallic implant materials, Mater. Sci. Eng., C 62 (2016) 249–259.
[33] E.J. Wladis, V.K. Aakalu, R.K. Sobel, M.T. Yen, J.R. Bilyk, L.A. Mawn, Orbital implants in enucleation surgery: a report by the American academy of ophthalmology, Ophthalmology 125 (2018) 311–317.
[34] C. Yang, H. Ma, Z. Wang, M.R. Younis, C. Liu, C. Wu, et al., 3D printed wesselsite nanosheets functionalized scaffold facilitates NIR-II photothermal therapy and vascularized bone regeneration, Adv. Sci. 8 (2021) e2100894.
[35] M. Isik, E. Karakaya, T.S. Arslan, D. Atila, Y.K. Erdogan, Y.E. Arslan, et al., 3D printing of extracellular matrix-based multicomponent, all-natural, highly elastic, and functional materials toward vascular tissue engineering, Adv. Healthcare Mater. 12 (2023) e2203044.
[36] J. Xie, X. Yang, H. Shao, J. Ye, Y. He, J. Fu, et al., Simultaneous mechanical property and biodegradation improvement of wollastonite bioceramic through magnesium dilute doping, J. Mech. Behav. Biomed. Mater. 54 (2016) 60–71.
[37] J. Wang, Y. Peng, M. Chen, X. Dai, L. Lou, C. Wang, et al., Next-generation finely controlled graded porous antibacterial bioceramics for high-efficiency vascularization in orbital reconstruction, Bioact. Mater. 16 (2022) 334–345.
[38] Z. Zhang, Y. Wang, W. Teng, X. Zhou, Y. Ye, H. Zhou, et al., An orthobiologics-free strategy for synergistic photocatalytic antibacterial and osseointegration, Biomaterials 274 (2021) 120853.
[39] X.Y. Chen, X. Yang, X.L. Fan, The evolution of orbital implants and current breakthroughs in material design, selection, characterization, and clinical use, Front. Bioeng. Biotechnol. 9 (2021) 800998.
[40] F. Baino, I. Potestio, Orbital implants: state-of-the-art review with emphasis on biomaterials and recent advances, Mater. Sci. Eng., C 69 (2016) 1410–1428.
[41] Y. Ramaswamy, C. Wu, H. Zhou, H. Zreiqat, Biological response of human bone cells to zinc-modified Ca-Si-based ceramics, Acta Biomater. 4 (2008) 1487–1497.
[42] S. Sauro, A. Babbar, B. Gharibi, V.P. Feitosa, R.M. Carvalho, L.K. Azevedo Rodrigues, et al., Cellular differentiation, bioactive and mechanical properties of experimental light-curing pulp protection materials, Dent. Mater 34 (2018) 868–878.
[43] G. Wang, Z. Lu, D. Dwarte, H. Zreiqat, Porous scaffolds with tailored reactivity modulate in-vitro osteoblast responses, Mater. Sci. Eng., C 32 (2012) 1818–1826.
[44] W.C. Hsu, J.P. Green, M.H. Spilker, P.A. Rubin, Primary placement of a titanium motility post in a porous polyethylene orbital implant: animal model with quantitative assessment of fibrovascular ingrowth and vascular density, Ophthalmic Plast. Reconstr. Surg. 16 (2000) 370–379.
[45] F. Baino, S. Perero, S. Ferraris, M. Miola, C. Balagna, E. Verné, et al., Biomaterials for orbital implants and ocular prostheses: overview and future prospects, Acta Biomater. 10 (2014) 1064–1087.
[46] J. Ye, J. He, C. Wang, K. Yao, Z. Gou, Copper-containing mesoporous bioactive glass coatings on orbital implants for improving drug delivery capacity and antibacterial activity, Biotechnol. Lett. 36 (2014) 961–968.
[47] T. Päällysaho, K. Tervo, T. Kivelä, I. Virtanen, A. Tarkkanen, T. Tervo, Cellular fibronectin and tenascin in an orbital nylon prosthesis removed because of infection caused by Staphylococcus aureus, Graefe's archive for clinical and experimental ophthalmology = Albrecht von Graefes Archiv fur klinische und experimentelle Ophthalmologie 231 (1993) 61–65.
[48] J. Wang, C. Wang, K. Jin, X. Yang, L. Gao, C. Yao, et al., Simultaneous enhancement of vascularization and contact-active antibacterial activity in diopside-based ceramic orbital implants, Mater. Sci. Eng., C 105 (2019) 110036.
[49] D. He, C. Zhuang, C. Chen, S. Xu, X. Yang, C. Yao, et al., Rational design and fabrication of porous calcium-magnesium silicate constructs that enhance angiogenesis and improve orbital implantation, ACS Biomater. Sci. Eng. 2 (2016) 1519–1527.
[50] Y. Li, T. Ma, X. Zhu, M. Zhang, L. Zhao, P. Wang, Zinc improves neurological recovery by promoting angiogenesis via the astrocyte-mediated HIF-1α/VEGF signaling pathway in experimental stroke, CNS Neurosci. Ther. 28 (2022) 1790–1799.
[51] Y. Song, H. Wu, Y. Gao, J. Li, K. Lin, B. Liu, et al., Zinc silicate/nano-hydroxyapatite/collagen scaffolds promote angiogenesis and bone regeneration via the p38 MAPK pathway in activated monocytes, ACS Appl. Mater. Interfaces 12 (2020) 16058–16075.

[52] Z. Zhang, W. Li, Y. Liu, Z. Yang, L. Ma, H. Zhuang, et al., Design of a biofluid-absorbing bioactive sandwich-structured Zn-Si bioceramic composite wound dressing for hair follicle regeneration and skin burn wound healing, Bioact. Mater. 6 (2021) 1910–1920.
[53] X. Yuan, T. Wu, T. Lu, J. Ye, Effects of zinc and strontium doping on in vitro osteogenesis and angiogenesis of calcium silicate/calcium phosphate cement, ACS Biomater. Sci. Eng. 9 (10) (2023) 5761–5771.
[54] K.A. Hing, S.M. Best, K.E. Tanner, W. Bonfield, P.A. Revell, Mediation of bone ingrowth in porous hydroxyapatite bone graft substitutes, J. Biomed. Mater. Res. 68 (2004) 187–200.
[55] P. Habibovic, H. Yuan, C.M. van der Valk, G. Meijer, C.A. van Blitterswijk, K. de Groot, 3D microenvironment as essential element for osteoinduction by biomaterials, Biomaterials 26 (2005) 3565–3575.
[56] P.A. Rubin, J.K. Popham, J.R. Bilyk, J.W. Shore, Comparison of fibrovascular ingrowth into hydroxyapatite and porous polyethylene orbital implants, Ophthalmic Plast. Reconstr. Surg. 10 (1994) 96–103.
[57] L.A. Cyster, D.M. Grant, S.M. Howdle, F.R. Rose, D.J. Irvine, D. Freeman, et al., The influence of dispersant concentration on the pore morphology of hydroxyapatite ceramics for bone tissue engineering, Biomaterials 26 (2005) 697–702.
[58] R.J. Kant, K.L.K. Coulombe, Integrated approaches to spatiotemporally directing angiogenesis in host and engineered tissues, Acta Biomater. 69 (2018) 42–62.